The E3 ubiquitin ligase adaptor *Tango10* links the core circadian clock to neuropeptide and behavioral rhythms

Jongbin Lee[a,b,c,1], Chunghun Lim[a,c,1], Tae Hee Han[a,2], Tomas Andreani[a], Matthew Moye[d,3], Jack Curran[a], Eric Johnson[e], William L. Kath[e], Casey O. Diekman[d], Bridget C. Lear[a], and Ravi Allada[a,4]

[a]Department of Neurobiology, Northwestern University, Evanston, IL 60208; [b]Department of Biological Sciences, Korea Advanced Institute of Science and Technology, Daejeon 34141, Republic of Korea; [c]Department of Biological Sciences, Ulsan National Institute of Science and Technology, Ulsan 44919, Republic of Korea; [d]Department of Mathematical Sciences, New Jersey Institute of Technology, Newark, NJ 07102; and [e]Department of Engineering Sciences and Applied Math, Northwestern University, Evanston, IL 60208

Edited by Joseph S. Takahashi, The University of Texas Southwestern Medical Center, Dallas, TX, and approved October 6, 2021 (received for review June 14, 2021)

Circadian transcriptional timekeepers in pacemaker neurons drive profound daily rhythms in sleep and wake. Here we reveal a molecular pathway that links core transcriptional oscillators to neuronal and behavioral rhythms. Using two independent genetic screens, we identified mutants of *Transport and Golgi organization 10* (*Tango10*) with poor behavioral rhythmicity. *Tango10* expression in pacemaker neurons expressing the neuropeptide PIGMENT-DISPERSING FACTOR (PDF) is required for robust rhythms. Loss of *Tango10* results in elevated PDF accumulation in nerve terminals even in mutants lacking a functional core clock. TANGO10 protein itself is rhythmically expressed in PDF terminals. Mass spectrometry of TANGO10 complexes reveals interactions with the E3 ubiquitin ligase CULLIN 3 (CUL3). CUL3 depletion phenocopies *Tango10* mutant effects on PDF even in the absence of the core clock gene *timeless*. Patch clamp electrophysiology in *Tango10* mutant neurons demonstrates elevated spontaneous firing potentially due to reduced voltage-gated Shaker-like potassium currents. We propose that *Tango10/Cul3* transduces molecular oscillations from the core clock to neuropeptide release important for behavioral rhythms.

circadian rhythms | neuronal output | ubiquitin ligase | *Drosophila* | potassium current

Circadian (~24 h) clocks govern almost all aspects of behavior and physiology across the animal kingdom. These overt daily behavioral rhythms are driven by oscillatory transcriptional feedback loops whose components are modified by phosphorylation and ubiquitination. In *Drosophila*, the CLOCK(CLK)-CYCLE (CYC) heterodimer activates transcription from *period* (*per*) and *timeless* (*tim*) promoters (1, 2). PER and TIM feedback to inhibit CLK-CYC activity and suppress their own transcription. CLK-CYC also activates activator *PAR-domain protein 1* (*Pdp1*) and repressor *vrille* (*vri*), which feedback to control *Clk* transcription (3, 4). Posttranscriptional control of core clock components also plays a crucial role in sustaining molecular clocks (5–10). Phosphorylation of clock proteins modulates their subcellular localization, activity, and susceptibility to ubiquitin-dependent degradation (11–16).

Core clock oscillations in about 150 networked pacemaker neurons are responsible for discrete aspects of rhythmic behavior. Of special importance are just 10 PDF-expressing pacemaker neurons (small ventral lateral neurons; sLNv), which are critical for free-running behavioral rhythms. The sLNv act as primary pacemakers in constant darkness (DD), synchronizing the circadian phase of molecular clocks among PDF- and non–PDF-expressing groups of clock neurons, including the dorsal lateral neurons (LNd) and the PDF-negative sLNv. Loss of PDF or PDF receptor (PDFR) result in dramatically reduced free-running rhythmicity, highlighting the crucial role of this neuropeptide (17–24).

The circadian clock also regulates multiple aspects of pacemaker neural output. Clock regulation promotes rhythmic accumulation of PDF levels (25) in part through *vri*, *no on or off transient A/complexin*, and the sodium leak channel *narrow abdomen* (*na*) (26–29). In addition, the clock also regulates daily structural rhythms in the sLNv axonal terminals, including changes in arborization and fasciculation (30). Structural plasticity rhythms may be mediated by clock transcriptional regulation of *vri*, *Myocyte enhancer factor 2* (*Mef2*)/*Fasciclin 2*, and *Puratrophin-1-like* (27, 31–34). Changes in structural plasticity appear to contribute to behavior under different environmental conditions, likely through changes in sensory inputs (34, 35). However, oscillations in structural plasticity or PDF levels are likely not essential for rhythmic behavior, as strains that lack these rhythms often retain strong behavioral rhythmicity (31, 33, 34, 36), suggesting other mechanisms play a role.

NEUROSCIENCE

Significance

In animals, the control of daily sleep–wake rhythms is mediated by discrete circadian clock neurons via their rhythmic activity–dependent release of neuropeptides and neurotransmitters. Here, we describe a gene, *Tango10*, critical for daily behavioral rhythms. TANGO10 functions as an adaptor with its partner, the E3 ubiquitin ligase CULLIN 3, to regulate protein ubiquitination, neuronal excitability via voltage-gated potassium channels, and neuropeptide accumulation. These studies define a mechanism for control of neuronal excitability and daily rhythmicity.

Author contributions: J.L., C.L., T.H.H., T.A., M.M., J.C., E.J., W.L.K., C.O.D., and R.A. designed research; J.L., C.L., T.H.H., T.A., M.M., J.C., and E.J. performed research; M.M., E.J., W.L.K., and C.O.D. contributed new reagents/analytic tools; J.L., C.L., T.H.H., T.A., M.M., J.C., E.J., W.L.K., C.O.D., B.C.L., and R.A. analyzed data; and J.L., C.L., T.H.H., T.A., M.M., J.C., E.J., W.L.K., C.O.D., B.C.L., and R.A. wrote the paper.

The authors declare no competing interest.

This article is a PNAS Direct Submission.

[1]J.L. and C.L. contributed equally to this work.

[2]Present address: Eunice Kennedy Shriver National Institute of Child Health and Human Development, National Institute of Health, Bethesda, MD 20892.

[3]Present address: Department of Quantitative Pharmacology & Pharmacometrics (QP2), Merck & Co. Inc., Kenilworth, NJ 07033.

[4]To whom correspondence may be addressed. Email: r-allada@northwestern.edu.

This article contains supporting information online at http://www.pnas.org/lookup/suppl/doi:10.1073/pnas.2110767118/-/DCSupplemental.

Published November 19, 2021.

Circadian neurons also exhibit daily rhythms in excitability (37–39), which may be mediated in part by clock regulation of the sodium leak channel regulator *Nlf-1* and the calcium-dependent potassium channel *Slowpoke* (30, 39, 40). Notably, acute or chronic hyperexcitation of PDF neurons elevates PDF levels and enhances defasciculation of the sLNv terminals (33, 41, 42), while acute silencing has opposing effects (43), indicating that changes in clock neuron excitability can affect PDF levels and sLNv morphology. Clock- and excitability-dependent arborization changes depend on PDF/PDFR, highlighting the critical role for this neuropeptide (27, 42). Here, we demonstrate that TANGO10-CUL3 defines a circadian output pathway important for regulating pacemaker neuron excitability and PDF levels. Loss of TANGO10-CUL3 severely disrupts free-running rhythmic behavior highlighting its crucial role in neuronal output.

Results

Loss of the BTB Adaptor Tango10 Strongly Reduces Free-Running Rhythms. Identification of clock mutants has been an essential strategy to understand how genetic components shape circadian behaviors and clock-relevant physiology. As part of a genetic screen (44), we identified a P-element insertion allele of *Tango10* (*Tango10*^{GG}) that strongly reduces behavioral rhythmicity, comparable to the strongest clock mutants reported (Fig. 1 *A* and *B* and *SI Appendix*, Fig. S1 and Table S1). *Tango10*^{GG} head extracts do not express detectable TANGO10 protein, consistent with a strong or complete loss-of-function allele (Fig. 1*C* and *SI Appendix*, Fig. S2). Females transheterozygous for *Tango10*^{GG} and chromosomal deletions of the *Tango10* locus display poor rhythmic power similar to hemizygous male flies (Fig. 1*D* and *SI Appendix*, Table S1). Importantly, excision of the P element or transgenic expression of a genomic *Tango10* construct fully reverts/rescues the circadian arrhythmicity of *Tango10*^{GG} mutants (Fig. 1*E* and *SI Appendix*, Table S2).

We independently identified a mutant through an X chromosome ethyl methanesulfonate (EMS) mutagenesis screen for disruptions in circadian and sleep behaviors. We named this mutant *busy run* (*bsr*), based on a Korean word meaning "diligent" and pronounced as [bu:zirʌn]. *bsr* mutants display arrhythmic locomotor behavior in DD comparable to *Tango10*^{GG} mutants (Fig. 1*A* and *SI Appendix*, Table S1). Complementation tests revealed that neither *Tango10*^{GG} nor genomic

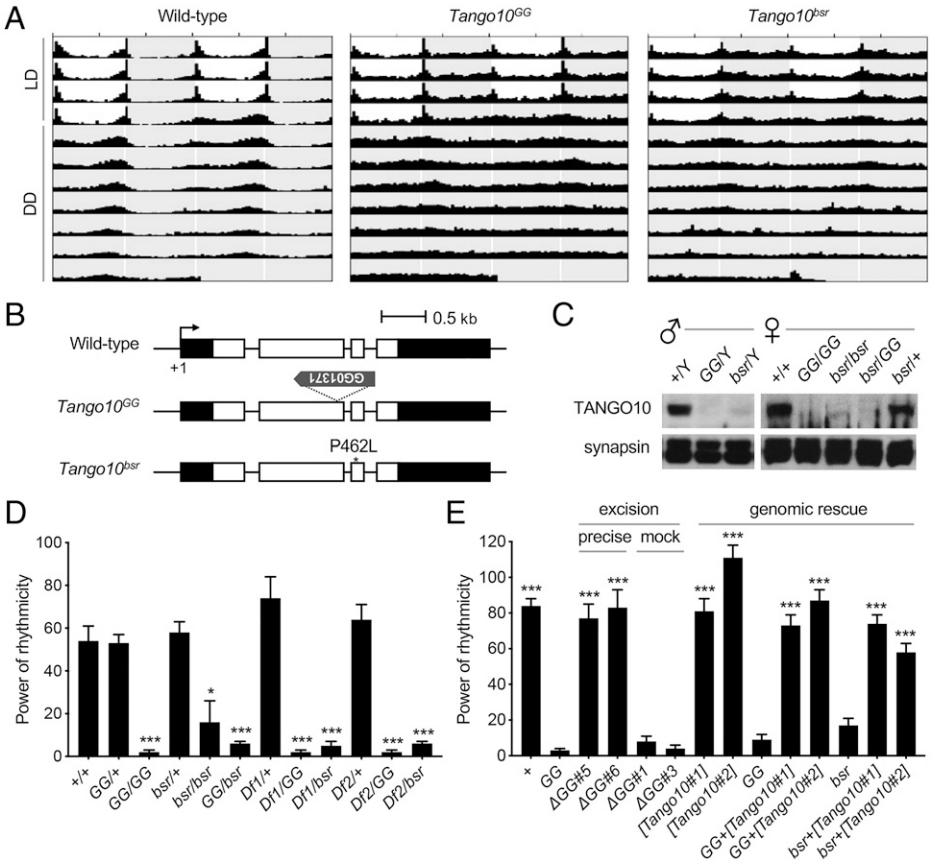

Fig. 1. Loss of *Tango10* disrupts behavioral rhythms. (*A*) Average activity profiles of WT and *Tango10* mutant strains during 4 d LD (white and gray background) followed by 7 d DD (gray background). White, light phase; gray, dark phase. n = 34 to 59. (*B*) Schematic diagrams of the *Tango10* locus and mutant alleles. Black boxes, untranslated regions; white boxes, coding sequences. The *Tango10*^{GG} mutant strain contains a P-element insertion within a coding exon (exon 2), while *Tango10*^{bsr} contains an EMS-mediated missense mutation in exon 3 (P462L), marked with an asterisk. (*C*) Protein extracts from WT, *Tango10* mutant, and heterozygous flies blotted with rat anti-TANGO10 and anti-synapsin as loading control. GG indicates *Tango10*^{GG} mutant, while *bsr* refers to the *Tango10*^{bsr} mutant. Uncropped images were shown in *SI Appendix*, Fig. S2*A*. (*D* and *E*) Locomotor rhythmicity, as determined by χ^2 periodogram analysis over 7 d of DD. Error bars indicate SEM. (*D*) Complementation rhythmicity data from adult female strains as indicated. Df1 refers to *Df(1)ED7147*, while Df2 refers to *Df(1)BSC722* (n = 8 to 51). Statistical significance determined using one-way ANOVA followed by Dunnett's comparison test or two-way ANOVA followed by Tukey's multiple comparison test, with comparisons made to WT control (***$P < 0.001$, *$P < 0.05$). (*E*) Excision and genomic rescue rhythmicity data from the adult male strains indicated. ΔGG indicates precise (#5 and #6) or mock (#1 and #3) excision strains. [*Tango10*#1] and [*Tango10*#2] indicate *Tango10* genomic rescue transgenes (n = 12 to 71). Statistical comparisons made using one-way ANOVA followed by Dunnett's test (excision) or two-way ANOVA followed by Tukey's multiple comparison test (genomic rescue). Asterisks indicated significant difference from corresponding mutant (*Tango10*^{GG} *or Tango10*^{bsr}) (***$P < 0.001$) (*SI Appendix*, Tables S1 and S2).

deletions spanning the *Tango10* locus rescue *bsr* mutant phenotypes in transheterozygous females (Fig. 1*D* and *SI Appendix*, Table S1), suggesting that *bsr* might be a recessive mutant allele of *Tango10*. To assess this possibility, we compared the coding sequences of *Tango10* in wild-type (WT) and *bsr* mutants. Indeed, we found a missense mutation in *bsr* mutants that converts phenylalanine at the position of amino acid 462 to leucine (P462L) within the third coding exon of *Tango10* (Fig. 1*B* and *SI Appendix*, Fig. S3*A*). Sequence alignments reveal strong conservation of this residue among TANGO10 homologs including human (*SI Appendix*, Fig. S3*B*), implicating its significance in the structure, stability, or function of TANGO10 proteins. Consistent with this hypothesis, we find that TANGO10 proteins are barely detectable in head extracts of *bsr* mutants (Fig. 1*C* and *SI Appendix*, Fig. S2). Finally, a genomic transgene harboring a WT *Tango10* locus fully rescues the circadian phenotypes in *bsr* mutants (Fig. 1*E* and *SI Appendix*, Table S2). Taken together, these genetic data convincingly demonstrate that *Tango10* is a clock gene whose importance for sustaining high-amplitude rhythms is comparable to core clock genes.

Tango10 Function in PDF Neurons Is Necessary to Drive Free-Running Rhythms. To determine the anatomical requirements for *Tango10*, we employed GAL4-UAS to express WT *Tango10* complementary DNA in *Tango10*^{GG} mutants in specific tissues and stages. We find that adult-specific *Tango10* induction using the RU486 inducible GeneSwitch system either pan-neuronally or ubiquitously (*elav-geneswitch*-GAL4 or *daughterless-geneswitch*-GAL4, respectively) restores robust behavioral rhythms in *Tango10* mutants, indicating that *Tango10* functions in adult neurons (Fig. 2*A* and *SI Appendix*, Table S3). In contrast, *Tango10* expression in all (*tim*-GAL4) or subsets of (*Clk*-GAL4, *Pdf*-GAL4) circadian pacemaker neurons does not rescue *Tango10* mutant rhythms (Fig. 2*B* and *SI Appendix*, Table S4). The lack of rescue using circadian drivers cannot be attributed to overexpression, as *Tango10* overexpression with these circadian drivers in a WT background does not reduce rhythmicity (*SI Appendix*, Table S4), suggesting that *Tango10* may function in nonclock neurons to sustain free-running locomotor rhythms.

To narrow down the anatomical locus necessary for *Tango10*-dependent clocks, we combined broader GAL4 rescue with different GAL80 transgenes to block GAL4 induction in defined subsets of neurons. We used the broadly expressing GAL4, 30Y-GAL4 (45), which robustly rescues rhythmicity in *Tango10* mutants (Fig. 2*B* and *SI Appendix*, Table S4). 30Y-driven *Tango10* rescue is blocked using the pan-neuronal *elav*-GAL80, confirming a neuronal *Tango10* requirement (Fig. 2*C* and *SI Appendix*, Table S4). 30Y is notably active in mushroom body (MB) neurons (45), yet the MB-specific GAL80, *247*-GAL80, does not block rescue. On the other hand, blocking 30Y specifically in PDF neurons did substantially suppress rescue of behavioral rhythms (Fig. 2*C* and *SI Appendix*, Table S4). Thus, *Tango10* function in PDF neurons is necessary to drive free-running rhythms.

To validate the necessity of *Tango10* in PDF neurons, we silenced endogenous *Tango10* expression in the select neurons by RNA interference (RNAi) and examined effects on circadian locomotor rhythms. We first confirmed that pan-neuronal expression of the *Tango10* RNAi transgene effectively depletes endogenous TANGO10 proteins in fly head extracts, indicating RNAi efficacy and neuronal TANGO10 expression (*SI Appendix*, Fig. S4). We further found that *Tango10* depletion in PDF neurons but not in MB neurons leads to behavioral

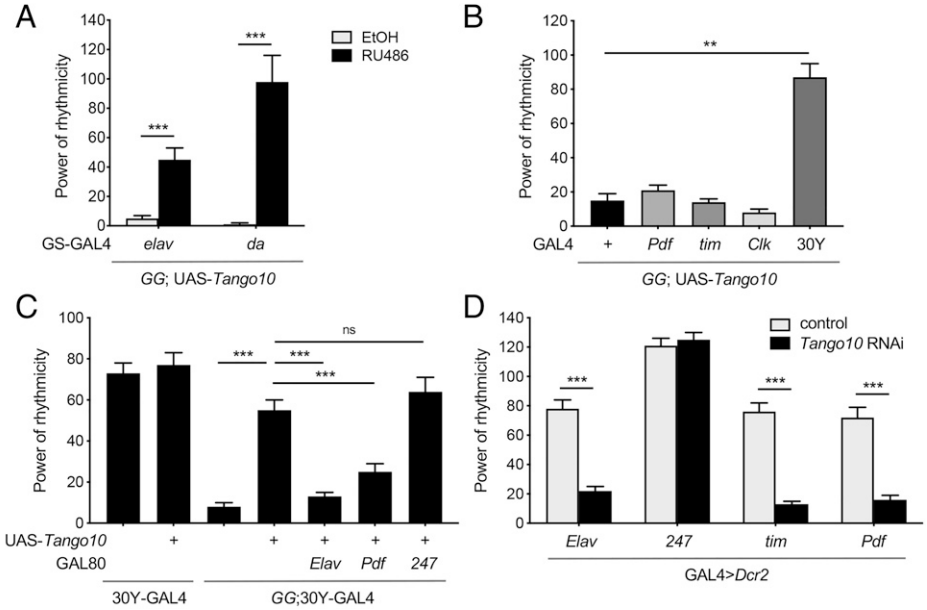

Fig. 2. *Tango10* expression in PDF neurons and adult stage–specific expression are important for sustaining rhythmic behavior. Assessment of behavioral rhythmicity in *Tango10* mutant, rescue, and RNAi strains, as determined using χ^2 periodogram analysis. *GG* indicates *Tango10* ^{GG} mutant allele. Error bars indicate SEM. (*A*) Adult-specific expression of *Tango10* in *Tango10*^{GG} mutants, using *elav-GeneSwitch*-GAL4 (*elav*-GS-GAL4) and *daughterless-GeneSwitch*-GAL4 (*da*-GS-GAL4). Flies in which *Tango10* expression is induced in adulthood (RU486) exhibit increased behavioral rhythmicity compared to ethanol (EtOH, vehicle control)-fed flies (n = 8 to 22). Statistical significance determined by Student's t test (***P < 0.001). (*B*) 30Y-GAL4–driven *Tango10* expression restored rhythmicity of *Tango10*^{GG} mutants in contrast to circadian GAL4s including *Pdf*-GAL4, *tim*-GAL4, and *Clk*-GAL4 (n = 19 to 34). Statistical significance between GAL4 crossed lines and iso31 crossed control was determined by Student's t test (**P < 0.01). (*C*) *elav*- and *Pdf*-GAL80 blocked the rescue of rhythmicity by 30Y-GAL4 driven *Tango10* expression (n = 15 to 39). Statistical significance was determined by one-way ANOVA with Dunnett's multiple comparisons test. (ns, not significant; ***P < 0.001). (*D*) RNAi-mediated TANGO10 depletion in clock neurons phenocopies *Tango10*^{GG} mutants. UAS-*Dicer2* was combined with GAL4 driver (GAL4>*Dcr2*) to increase RNAi efficiency (n = 32 to 44). Statistical significance was determined using one-way ANOVA followed by Dunnett's test ***P < 0.001) (*SI Appendix*, Tables S3 and S4).

arrhythmicity, comparable to that of *Tango10* mutants (Fig. 2*D* and *SI Appendix*, Table S4). Taken together, these data demonstrate that *Tango10* in PDF neurons is necessary but not sufficient for robust rhythmicity in circadian locomotor behavior.

Loss of Tango10 Function Selectively Affects Small LNv PER and TIM Oscillations. Daily rhythmic expression of clock proteins underlies circadian locomotor behavior. We thus examined the daily expression of core clock proteins PER and TIM as a measure of molecular clocks. Immunoblotting of adult head extracts at circadian time (CT) 3 and CT15 showed comparable levels of PER and TIM between WT and *Tango10* mutants (*SI Appendix*, Fig. S5). We also evaluated PER and TIM rhythms in light:dark (LD) cycle (i.e., 12-h light: 12-h dark) in individual groups of circadian pacemaker neurons: PDF+ sLNv and large LNv (lLNv) and PDF- LNd and fifth sLNv (Fig. 3). PER and TIM oscillations were evident in all groups of neurons in both WT and *Tango10* mutants (Fig. 3). Moreover, in most of those groups, levels and oscillation amplitude were comparable between WT and *Tango10* mutants, although modest time-dependent changes in protein levels are consistent with a small phase delay in *Tango10* mutants (Fig. 3). *Tango10* sLNv exhibit the most prominent effects, with a modest ~30% reduction in peak PER levels (2.5× oscillation in WT and 1.9× in *Tango10*) and a ~60% reduction in TIM levels, although TIM levels still oscillate significantly (~3×; Fig. 3). Similar results were obtained in free-running DD when circadian locomotor rhythms disappear in *Tango10* mutants (*SI Appendix*, Fig. S6).

Loss of Tango10 Dramatically Elevates PDF Levels in Clock Neuron Terminals. The finding of persistent but reduced amplitude molecular oscillations suggests that *Tango10* may function to regulate the output of PDF neurons. The molecular clock is thought to transmit timing information in part via the daily rhythm in the circadian neuropeptide PDF. To assess *Tango10* effects on PDF, we examined PDF accumulation at the dorsal axonal terminals of the sLNv. WT sLNv display robust PDF rhythms, with the peak levels 2 h after lights-on in LD cycle (i.e., zeitgeber time [ZT] 2; lights-on at ZT0; lights-off at ZT12) (Fig. 4 *A* and *B*) (25). *Tango10* mutant sLNv, however, displayed constitutively high PDF levels at their axon terminals, dampening PDF rhythms in both LD cycle (Fig. 4 *A* and *B*) and DD (*SI Appendix*, Fig. S7). Moreover, the structural rhythmicity in sLNv terminals was dampened by *Tango10* mutation, whereas *Tango10* sLNv cell bodies displayed PDF oscillations comparable to WT (Fig. 4 *C* and *D*). *Tango10* effects on PDF levels were also detected at lLNv terminals in the optic lobe since *Tango10* lLNv displayed no significant changes in terminal PDF levels (*SI Appendix*, Fig. S8). Given that the circadian clock regulates PDF levels at sLNv terminals (25) and *Tango10* impacts TIM levels, we wondered if high PDF levels in *Tango10* mutant sLNv required *tim*. Accordingly, we generated double mutants of $Tango10^{GG}$ and tim^{01} and examined their PDF expression. We found that loss of *Tango10* results in elevated PDF levels even in a *tim* null mutant background (Fig. 4*E*), indicating *tim* is not required for *Tango10* regulation of PDF.

We next examined the subcellular localization of TANGO10 to determine how it might exert loss-of-function effects on PDF. Unfortunately, our anti-TANGO10 antibody failed to detect endogenous TANGO10 proteins in whole-mount brains by immunostaining. We thus expressed transgenic TANGO10 proteins with an HA epitope-tag in order to visualize expression in PDF neurons. We confirmed that the *Tango10-HA* transgene strongly rescues *Tango10* mutant rhythms indicating it is functional (Fig. 5*A*). When expressed in PDF neurons, transgenic TANGO10-HA exhibits punctate localization in the axonal tract and terminals of sLNv neurons (Fig. 5*B*). We observe partial colocalization between PDF and TANGO10-HA expression in

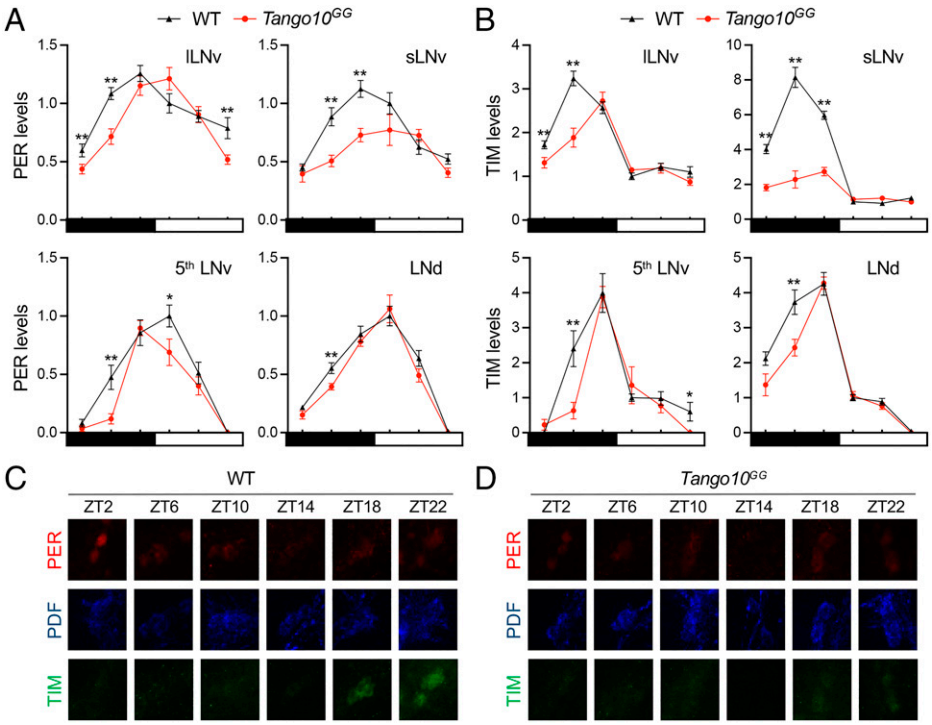

Fig. 3. Clock oscillations are dampened in *Tango10* mutant sLNv. (*A* and *B*) PER and TIM levels were quantified from individual groups of circadian pacemaker neurons during the LD cycle. Averaged intensity in WT at ZT 2 was set as 1 for normalization. Data represent means ± SEM (n = 14 to 18 hemispheres from two experiments). WT and *Tango10* measurements were compared at each time-point using Student's t test (*$P < 0.05$, **$P < 0.01$). lLNv, large ventral lateral neuron; sLNv, small ventral lateral neuron; fifth LNv, PDF-negative LNv; LNd, dorsal lateral neuron. (*C* and *D*) Representative confocal images of WT and $Tango10^{GG}$ mutant sLNv.

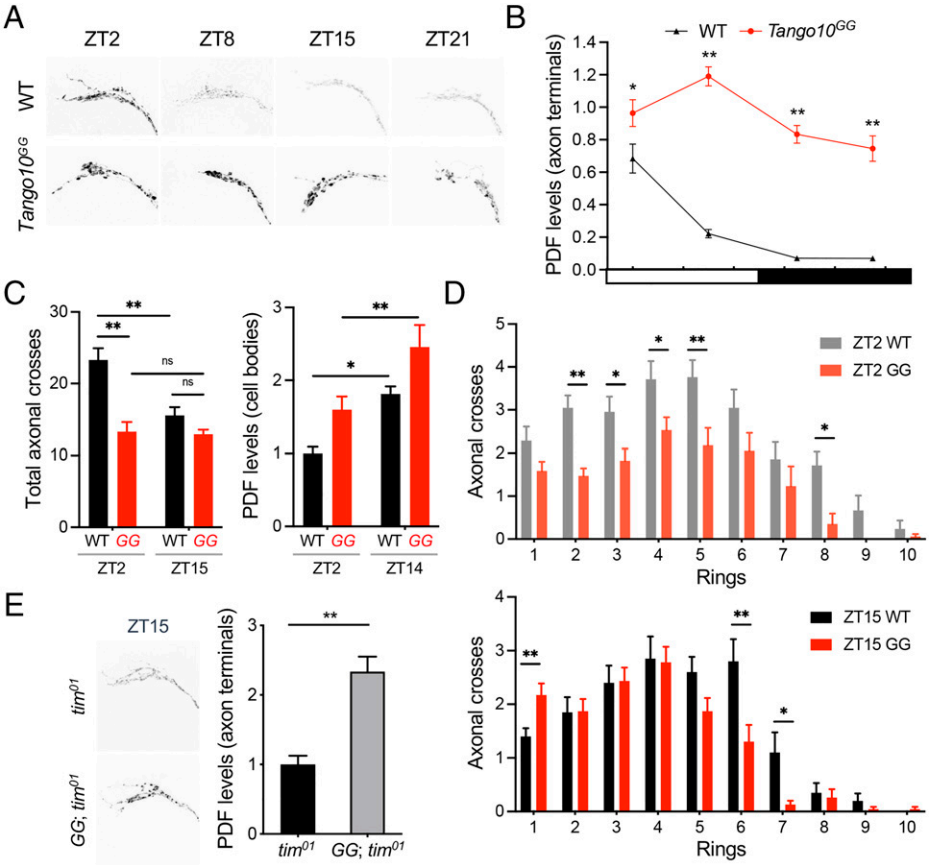

Fig. 4. Loss of *Tango10* results in elevated PDF in the absence of *tim*. (*A*) Representative *z*-stacked maximum intensity projection images of PDF staining in dorsal terminals of sLNv under LD conditions. ZT, zeitgeber time. (*B*) Quantification of PDF intensity in sLNv dorsal projection. Section images were stacked as maximum intensity projection. Integrated intensities above a threshold were measured and normalized to averaged measurement of *Tango10*^{GG} mutant at ZT2 (set as 1). Data represent means ± SEM (n = 14 to 22 hemispheres from two experiments). WT and *Tango10* measurements were compared at each time point using Student's *t* test (*P < 0.05, **P < 0.01). (*C*) Quantification of sLNv arborization in dorsal projections (*Left*) and PDF expression in sLNv cell bodies (*Right*). Axonal crosses were measured using Sholl analysis. PDF intensity in sLNv cell bodies was normalized to averaged measurement of WT at ZT2 (set as 1). GG indicates *Tango10*^{GG} mutant. Data represent means ± SEM (n = 17 to 23 hemispheres for sLNv arborization; n = 16 to 18 hemispheres for sLNv cell bodies). Two-way ANOVA detected significant genotype× time point interaction effects on total axonal crosses in sLNv dorsal projections (P = 0.0037) but not on PDF levels in sLNv cell bodies (P = 0.8904), whereas *Tango10* effects on both measurements were significant (P < 0.0001 and P = 0.0010, respectively). ns, not significant; *P < 0.05, **P < 0.01, as determined by Tukey's post hoc test. (*D*) Axonal crosses for each concentric ring were analyzed in WT and *Tango10*^{GG} mutant sLNv. Data represent means ± SEM (n = 17 to 23 hemispheres from two experiments). *P < 0.05, **P < 0.01 as determined by Student's *t* test. (*E*) Representative images and quantification of anti-PDF signals in dorsal projections of *tim*^{01} or *Tango10*^{GG} *tim*^{01} mutant sLNv at ZT15. Integrated intensities for anti-PDF staining above a threshold were measured and normalized to averaged measurement of *tim*^{01} mutant (set as 1). Data represent means ± SEM (n = 22 to 24). **P < 0.01 as determined by Student's *t* test.

the sLNv terminals, with TANGO10 exhibiting somewhat broader localization (Fig. 5*B*). Moreover, our quantitative analysis revealed robust TANGO10 rhythms at axonal terminals of sLNv in LD cycles (Fig. 5 *C* and *D*; peak ZT10, trough ZT22). These data suggest that rhythmic TANGO10 expression in the dorsal terminals is downstream of the circadian clock and, in turn, may contribute to rhythmic PDF levels.

Proteomic Analysis Identifies CUL3 as a TANGO10-Interacting Partner. Multiple sequence alignments indicate that BTB/POZ and BACK domains implicated in protein-protein interactions are well conserved among TANGO10 homologs (*SI Appendix*, Fig. S3*B*). Accordingly, we performed proteomic analyses of immunoprecipitated TANGO10 protein complexes from fly heads to identify factors mediating *Tango10*-dependent clock function in vivo. We first confirmed that a C-terminal triple FLAG tag does not interfere with WT *Tango10* function as pan-neuronal expression of the FLAG-tagged TANGO10 rescues behavioral phenotypes in *Tango10* mutants (*SI Appendix*, Table S5). We expressed FLAG-tagged TANGO10 either in WT clock cells using *tim*-GAL4 or in all postmitotic neurons using *elav*-GAL4. The protein complex associating with FLAG-tagged TANGO10 was then affinity purified by immunoprecipitation at ZT10 and ZT22 and analyzed by mass spectrometry. To identify "hits," we looked for proteins that were detected in at least two of the four samples but not present in GAL4/+ controls nor in immunoprecipitation of the clock translation factor TWENTY-FOUR (6). This strategy revealed 21 overlapping hits from independent proteomic analyses (*SI Appendix*, Table S6). Interestingly, an E3 ligase CUL3 was identified as one of the overlapping hits present in both *tim*-GAL4 samples and one out of two *elav*-GAL4 samples. CUL3 has been proposed to play a role in TIM ubiquitination, contributing to high-amplitude TIM cycling and behavioral rhythms (16, 46, 47). TANGO10 and CUL3 coimmunoprecipitate from *Drosophila* S2 cells when transiently transfected. (Fig. 6*A*). We also observed that endogenous CUL3 coimmunoprecipitates with *tim*-GAL4–driven FLAG-tagged TANGO10, further confirming their in vivo interactions (Fig. 6*B*). Taken together, these data suggest that TANGO10 and CUL3 form a protein complex to sustain circadian rhythms.

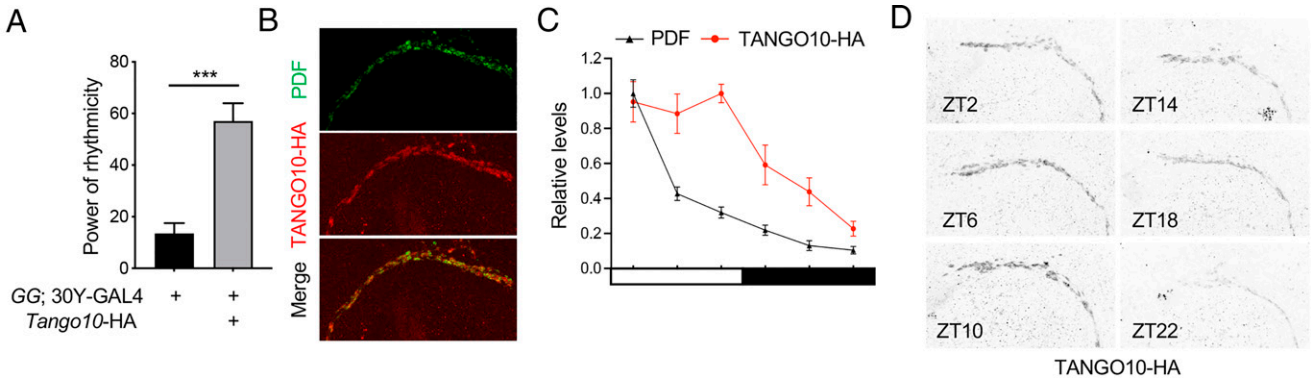

Fig. 5. Transgenic TANGO10 protein localizes to and oscillates in PDF neuron dorsal terminals. (*A*) 30Y-GAL4–driven *Tango10*-HA expression rescues behavioral rhythmicity in *Tango10*^{GG} mutants (GG), analyzed over 7 d DD using χ^2 periodogram analysis. Data represent means ± SEM (n = 16 to 24). ***P < 0.001 as determined by Student's t test. (*B*) Representative confocal images of sLNv dorsal terminals expressing PDF (green) and TANGO10-HA (red) at ZT 15. (*C* and *D*) *Pdf*-GAL4–driven TANGO10-HA cycles in the sLNv dorsal projections. Quantification of TANGO10-HA and PDF signals was performed as in Fig. 4. TANGO10-HA or PDF intensity at ZT2 was set to 1. Data represent means ± SEM (n = 27 to 38 from three independent experiments). TANGO10-HA cycling was detected by one-way ANOVA (P < 0.0001). Representative maximum intensity projection images of TANGO10-HA staining in *Pdf*-GAL4 UAS-*Tango10*-HA brains were shown.

CUL3 Depletion Phenocopies the Behavioral Rhythms and PDF Levels of Tango10 Mutants. To assess *Cul3* function in PDF neurons, we employed *Pdf*-GAL4–driven *Cul3* RNAi. We find that CUL3 depletion in PDF neurons severely dampens locomotor rhythms in free-running DD (Fig. 6*C* and *SI Appendix*, Table S7), consistent with a prior report (16). We next determined if *Cul3*, like *Tango10*, similarly affects PDF levels and find that PDF levels are constitutively high in the axon terminals of CUL3-depleted sLNv (Fig. 6 *D* and *E*), phenocopying the effects of *Tango10* mutants. Given the proposed links between CUL3 and TIM, we assessed *Cul3* effects in a *tim* null background (*tim*^{01}) and find elevated PDF levels similar to what we

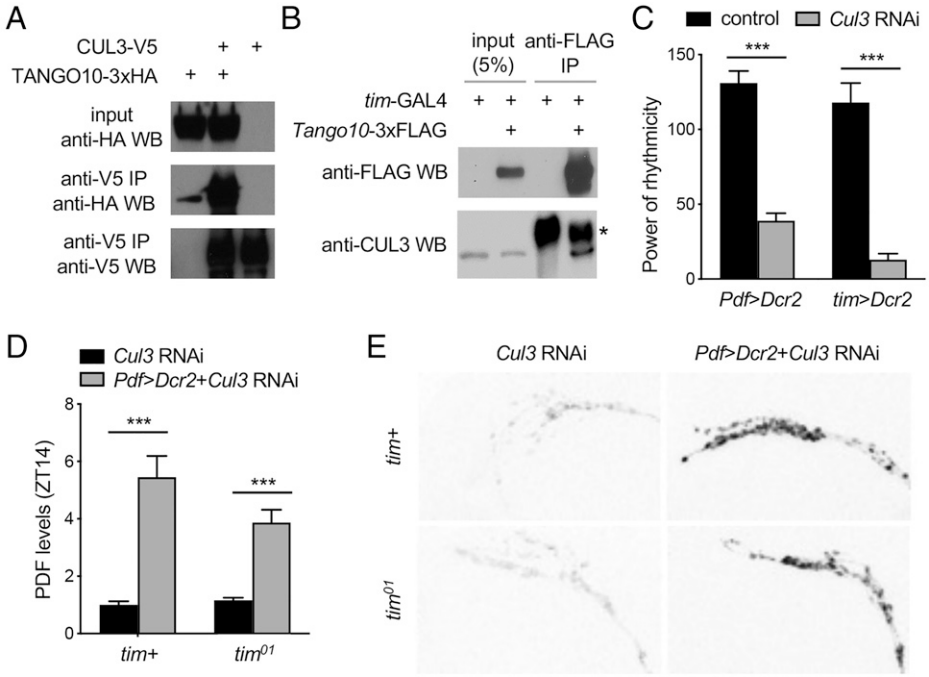

Fig. 6. Depletion of TANGO10 interactor CUL3 in PDF neurons phenocopies PDF expression phenotypes observed in *Tango10* mutants in the absence of *tim*. (*A*) Co-immunoprecipitation (IP) of CUL3 and TANGO10 in *Drosophila* S2 cells. Representative immunoblots of input and IP samples from S2 cells cotransfected with expression vectors for CUL3-V5 and TANGO10-HA as indicated. (*B*) Co-IP of CUL3 and TANGO10 in *Drosophila* heads. Immunoblotting analysis of input and IP samples from adult head extracts upon transgenic expression of FLAG-tagged TANGO10 using *tim*-GAL4, compared to *tim*-GAL4/+ control, assayed by anti-FLAG and anti-CUL3 antibodies. CUL3 is detected in input blots as well as IP blots for samples expressing FLAG-tagged TANGO10. The asterisk indicates nonspecific bands observed in both IP samples independent of *Tango10*-3xFLAG transgene, but the size of this band is larger than CUL3. (*C*) CUL3 depletion in circadian pacemaker neurons including PDF+ cells induces decreased rhythmicity. *Cul3* RNAi refers to NIG strain 11861R-2; *Pdf*>*Dcr2*, *Pdf*-GAL4 UAS-*Dcr2*; *tim*>*Dcr2*, *tim*-GAL4 UAS-*Dcr2*. Power of rhythmicity was determined using χ^2 periodogram. Data represent means ± SEM (n = 8 to 44). ***P < 0.001 as determined by Student's t test. See also *SI Appendix*, Table S7. (*D*) CUL3 depletion increases PDF intensity in sLNv dorsal projections at ZT 14 in the absence of *tim*. PDF signals were analyzed as in Fig. 4. Data represent means ± SEM (n = 14 to 16 from two independent experiments). Two-way ANOVA detected significant *Cul3* effects on PDF levels (P < 0.0001) but not their interaction with *tim* (P = 0.0599). ***P < 0.001 as determined by Tukey's multiple comparison test. (*E*) Representative PDF staining images of the dorsal projection from CUL3-depleted sLNv and RNAi control in a *tim*+ or *tim*^{01} background at ZT14.

observe for *Tango10* mutants (Fig. 6 *D* and *E*), supporting a role of *Cul3* on PDF in the absence of *tim*. The biochemical association and phenotypic similarity of *Cul3* and *Tango10* prompted us to hypothesize that CUL3 employs TANGO10 as an adaptor to drive PDF and behavioral rhythms downstream of the molecular clock.

Loss of Tango10 Increases Firing Rate and Depolarizes Membrane Potential. PDF levels in axonal terminals are also dependent on neuronal excitability (41, 42). To investigate the impact of a *Tango10* mutation on excitability, we performed whole-cell patch electrophysiology on the PDF-expressing lLNv. lLNv electrophysiology has been well-studied, as their position near the surface of the brain and large soma makes them more accessible compared to other fly clock neurons. We find that *Tango10* mutant lLNv exhibit increased excitability compared to WT (Fig. 7*A*). Firing frequency of *Tango10* lLNv is significantly higher compared to WT lLNv (Fig. 7*B*). The increase in firing rate of *Tango10* lLNv is linked to a more depolarized membrane potential (Fig. 7*C*, $P < 0.01$). Input resistance of lLNv was measured using a hyperpolarizing current injection protocol, with no significant difference found between WT and *Tango10* (Fig. 7*D*). Cell capacitance was determined from a current step measured in voltage-clamp mode, with *Tango10* lLNv neurons found to have a significantly lower capacitance compared to WT during morning hours (Fig. 7*E*). Nonetheless, the finding of elevated excitability in *Tango10* mutant neurons is consistent with a role in neuronal output.

4-AP–Sensitive I_A Potassium Current Is Significantly Reduced in Tango10 Mutant lLNv. To investigate which ion channels could be mediating the difference in *Tango10* mutant lLNv, we used voltage clamp electrophysiology. We observed a voltage-gated outward current with fast- and slow-inactivating components (Fig. 8*A*). We noted that the fast- but not slow-inactivating component was reduced in *Tango10* mutants (Fig. 8 *A*–*C*). We then used pharmacology to block subsets of potassium channels to further resolve the mechanisms underlying *Tango10* hyperexcitability. Whole-cell currents were recorded in the presence of tetrodotoxin (TTX) to block sodium channels, before repeating the same voltage-clamp protocol while adding tetraethylammonium (TEA) to block voltage-gated potassium channels. The TEA-sensitive current was calculated by subtracting the currents measured in the two conditions (Fig. 8*D*). No significant differences were found in the TEA-sensitive current between WT and *Tango10* (Fig. 8*E*). To further interrogate potassium channel currents, the same voltage-clamp protocol was performed with the further addition of 4-aminopyridine (4-AP) to the solution, with the 4-AP–sensitive current again calculated using subtraction of the currents evoked in the two conditions. Isolating the 4-AP–sensitive current revealed a significant reduction in *Tango10* lLNv (Fig. 8 *D* and *F*). The inactivation kinetics and pharmacological specificity of this current identifies a reduced Shaker-like (I_A) current in *Tango10* mutants.

To determine if reductions in I_A current can explain the increased firing rate observed in *Tango10* mutants, we developed a mathematical model of lLNv electrophysiology (*SI Appendix*, Table S8). Our model builds on the Smith model of

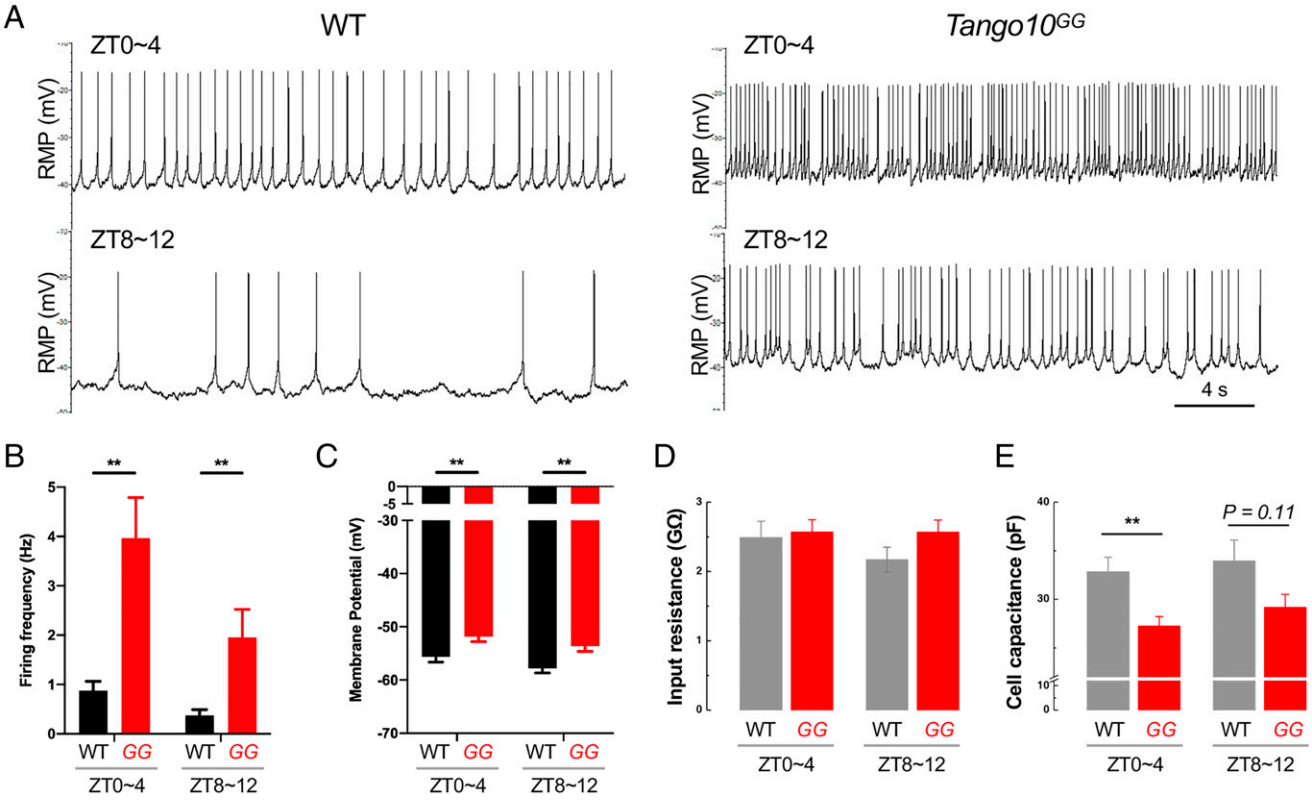

Fig. 7. Loss of *Tango10* increases excitability in PDF neurons. (*A*) Representative current-clamp recordings at ZT0~4 (*Top*) and ZT8~12 (*Bottom*) of WT (*Left*) and *Tango10*^{GG} (*Right*). (*B*) Summary bar graphs showing mean firing rate of WT (n = 18 at ZT0~4; n = 21 at ZT8~12) and *Tango10*^{GG} mutant (n = 19 at ZT0~4; n = 19 at ZT8~12). (*C*) Summary bar graphs showing mean membrane potential (MP) of WT (n = 18 at ZT0~4; n = 21 at ZT8~12) and *Tango10*^{GG} mutant (n = 19 at ZT0~4; n = 19 at ZT8~12). Data represent means ± SEM $^{**}P < 0.01$ as determined by Student's t test. (*D*) Input resistance was measured in current clamp from the voltage response to hyperpolarizing current steps. No difference was found between WT and *Tango10*^{GG} at both morning and evening (Student's t test). (*E*) Cell capacitance of *Tango10* mutant lLNv is significantly lower than WT at morning hours ($^{**}P < 0.01$) but not evening ($P = 0.11$), as determined by Student's t test.

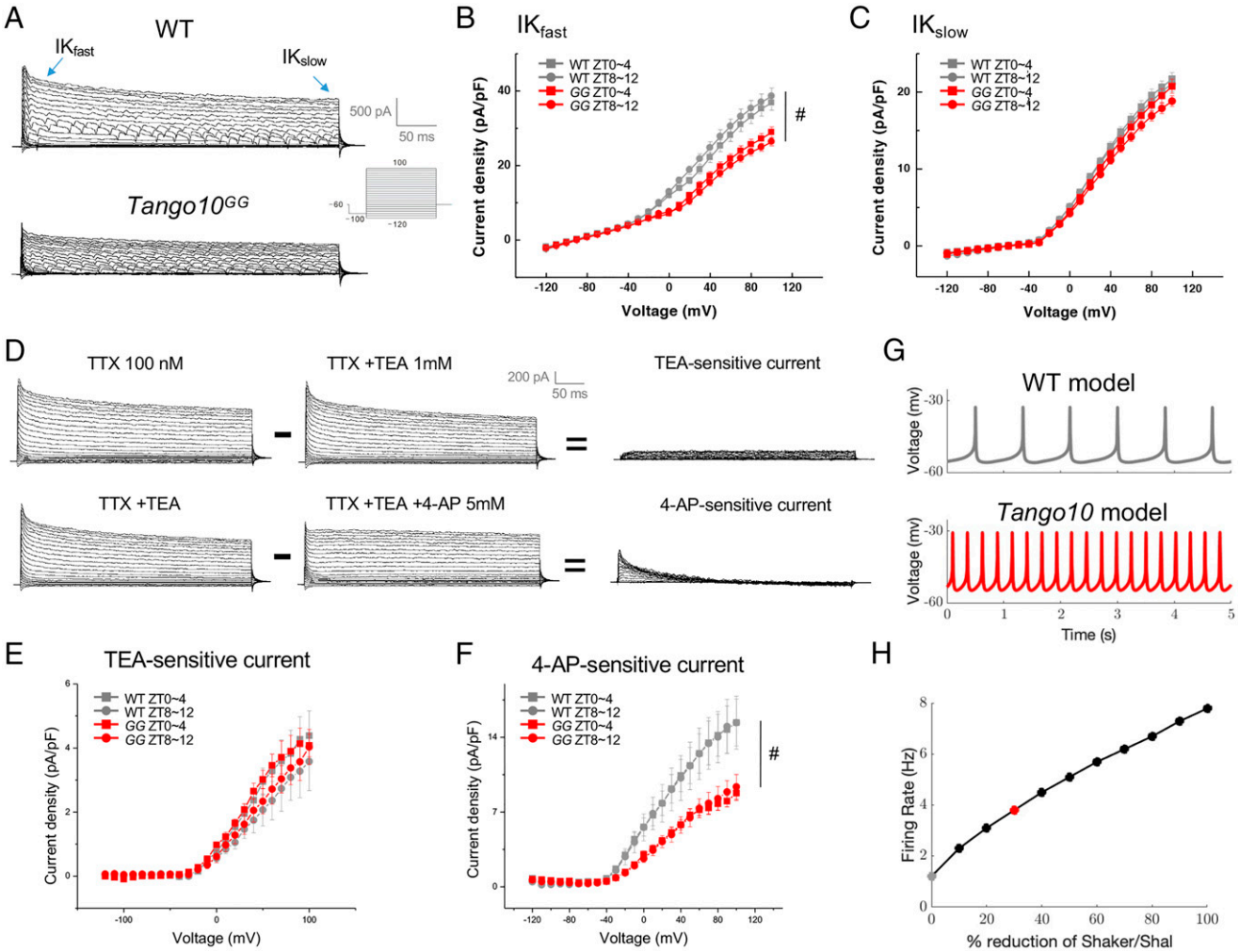

Fig. 8. Decreased I_A current in *Tango10* mutants may underlie increased firing rate. (*A*) Whole-cell current traces induced by step pulse to potentials between −120 and +100 mV with 10-mV increment in WT (*Top*) and *Tango10*^{GG} mutant (*Bottom*). Pulse protocols for recording whole-cell currents (*Inset*). (*B* and *C*) current-voltage plots show mean whole-cell current densities for the peak current (IK fast) and the late portion (IK slow) of the current of lLNv in WT (n = 14 at ZT0~4; n = 12 at 8~12) and *Tango10*^{GG} mutant (n = 17 at ZT0~4; n = 13 at ZT8~12). The amplitude of IK_{fast} current was significantly lower in *Tango10*^{GG} mutant lLNv compared with WT (two-way ANOVA, $P < 0.0001$). (WT ZT0~4 versus *GG* ZT0~4, WT ZT8~12 versus *GG* ZT8~12; $P < 0.05$ by two-way ANOVA; $^{\#}P < 0.05$, Tukey's honestly significant difference [HSD] test). (*D*) TEA-sensitive outward current (*Top* traces) and 4-AP–sensitive outward current (*Bottom* traces), respectively. (*E*) I-V show mean TEA-sensitive current densities of lLNv in WT (n = 7 at ZT0~4; n = 6 at 8~12) and *Tango10*^{GG} mutant (n = 5 at ZT0~4; n = 7 at ZT8~12). (*F*) I-V show mean 4-AP–sensitive current densities of lLNv in WT (n = 7 at ZT0~4; n = 6 at 8~12) and *Tango10*^{GG} mutant (n = 5 at ZT0~4; n = 7 at ZT8~12). The amplitude of 4-AP–sensitive current was significantly lower in *Tango10*^{GG} mutant lLNv compared with WT animal (two-way ANOVA, $P < 0.0001$) (WT ZT0~4 versus *GG* ZT0~4, WT ZT8~12 versus *GG* ZT8~12; $P < 0.05$ by two-way ANOVA; $^{\#}P < 0.05$, Tukey's HSD test). (*G*) Simulations of mathematical models of WT (*Top* trace, firing rate ~1 Hz) and *Tango10* mutant lLNv (*Bottom* trace, firing rate ~4 Hz). (*H*) Firing rate of model as a function of the percentage reduction in Shaker/Shal current, with red dot (30% reduction) and gray dot (0% reduction) corresponding to the *Tango10* and WT models shown in Fig. 8*G*, respectively.

lLNv (48), which includes an inward sodium current, an inward calcium current, a leak current, and four outward potassium currents: fast-inactivating A-type currents Shaker and Shal, and slow- or noninactivating currents Shab and Shaw. In the Smith model, the potassium current parameters were fit to voltage-clamp data isolating these currents in lLNv, whereas the sodium and calcium current parameters were taken from a previously published model of mammalian circadian clock neurons (49). For our model, we retained the Smith model potassium current parameters but refit the sodium and calcium current parameters to current-clamp data from lLNv using data assimilation (DA), a state and parameter estimation technique for optimally combining dynamical models with observations (*Materials and Methods*). This approach yielded a model that closely matches the firing rate and action potential (AP) shape observed in recordings from WT LNv (Fig. 8*G* and *SI Appendix*, Figs. S9 and S10). We then simulated the model with reduced values of the maximal conductance parameter for the Shaker and Shal currents. We found that a 30% reduction in Shaker/Shal currents can reproduce the increased firing rate phenotype of the *Tango10* mutants (Fig. 8 *G* and *H*).

To experimentally test the contribution of the TEA- and 4-AP–sensitive currents on lLNv neurophysiology, we measured the effects of pharmacological application of the respective drugs upon resting membrane potential, measured in the presence of TTX. Application of TEA resulted in a small depolarization of membrane potential (~1 to 2 mV), both at morning and evening, with no difference observed between *Tango10* and WT (*SI Appendix*, Fig. S11 *A* and *B*). However, application of 4-AP caused a larger depolarization (~5 to 10 mV) in WT lLNv, with a significantly smaller response in *Tango10* lLNv evident in the evening (*SI Appendix*, Fig. S11 *A* and *C*), providing further evidence for a

reduction of the 4-AP–sensitive current in *Tango10* lLNv. Interestingly, *Shal* gene expression and current levels are more elevated in the evening consistent with these 4-AP effects (48, 50).

Discussion

To discover genes involved in circadian behavior, we performed two large-scale genetic screens: one P-element–candidate based and the other an unbiased chemical mutagenesis. These divergent approaches independently identified mutants of *Tango10*, highlighting its pivotal role. These mutants profoundly disrupt free-running rhythmicity. Moreover, loss of *Tango10* results in dramatic accumulation of PDF in clock neuron terminals and loss of PDF accumulation rhythms. These effects persist in the absence of a functioning core clock. To better understand the molecular mechanisms by which *Tango10* functions, we analyzed TANGO10 complexes using immunoprecipitation and mass spectrometry and found interactions with the E3 ubiquitin ligase CUL3. CUL3 depletion also results in similar PDF accumulation effects. Patch clamp electrophysiology of PDF neurons demonstrates increased excitability and reduction of Shaker-like potassium currents suggesting that *Cul3*/*Tango10* effects are via elevated excitability. TANGO10 protein levels also oscillate in these terminals, suggesting they are under clock control and contribute to cellular rhythms. Taken together, this study reveals a critical ubiquitin–proteasome pathway by which temporal information is conveyed to cellular and behavioral outputs (*SI Appendix*, Fig. S12).

This work highlights a neuronal output pathway with remarkably robust effects on free-running circadian rhythms. Loss of *Tango10* with two independent alleles results in a substantial reduction in rhythmic power (~95% reduction in power-significance [P-S] for the GG allele). Independent alleles were discovered in two phenotype-driven screens. The strength of the rhythmicity phenotype is in contrast with those previously reported for loss-of-function alleles of other putative output genes. Much of the prominent work examining output in circadian neurons has focused on fasciculation/defasciculation of axonal arbors (33, 34). While the gold standard loss-of-function genetics (e.g., RNAi or dominant-negative manipulations) have profound consequences on rhythmic fasciculation neural states (see figure 1C in ref. 34) they have limited effects on the crucial functional output of these neurons, circadian behavior (see Fig. 4*D*; Rho1DN in ref. 34; and table 2 Pdf > Mef2 RNAi in ref. 33). The only studies that have observed large circadian behavioral phenotypes as a result of loss-of-function genetic manipulations are those targeting the PDF neuropeptide itself as well as subunits of the ion channel NA and its regulator NLF-1, which function via excitability (20, 39, 51). Our finding that *Tango10* has profound effects on free-running rhythmicity indicates it defines a special pathway crucial for free-running rhythmicity.

Using cell-type–specific genetic rescue and quantitative immunofluorescence, we demonstrate that *Tango10* effects on rhythmicity map to just ~20 clock neurons expressing the neuropeptide PDF. RNAi knockdown specifically in the LNv disrupts free-running rhythmicity, and LNv expression is required for robust rescue of the *Tango10* rhythmicity phenotype although *Tango10* in nonclock neurons further contributes to free-running rhythms. Additionally, the effects of *Tango10* and *Cul3* on the molecular clock are mainly observed in the sLNv group and not other pacemaker neuron groups (figure 3 in ref. 16). Taken together, our data indicate a critical functional requirement for TANGO10-CUL3 in the PDF-positive LNv to promote molecular and behavioral rhythmicity.

We have demonstrated that *Tango10* likely functions in concert with the E3 ubiquitin ligase CUL3, thus defining a role for protein ubiquitination in neuronal output. Proteomic and coimmunoprecipitation (Co-IP) experiments indicate that CUL3 and TANGO10 interact in vivo. Loss of *Tango10* or *Cul3* function in PDF neurons causes comparable arrhythmicity. Moreover, decreased *Tango10* or *Cul3* function also results in similar molecular phenotypes, including elevation of PDF levels even in the absence of *tim*. Ubiquitination can serve as a signal for protein degradation and/or traffic proteins to the cell membrane (52, 53). It will be of interest to examine the function of other TANGO10-interacting proteins as potential enzymatic targets of this complex.

Under this model (*SI Appendix*, Fig. S12), core clock effects observed may be secondary to *Tango10*-mediated effects on excitability/PDF. In most pacemaker neurons and in whole heads, PER and TIM oscillations are largely intact in *Tango10* mutants. We did observe modest reductions in peak PER levels and more robust reductions in TIM specifically in the sLNv. Interestingly, these sLNv phenotypes are very similar to those observed after *Cul3* impairments (16). This prior study proposed that CUL3 ubiquitinates TIM, targeting it for degradation. Yet loss of putatively TIM-degrading *Cul3* results in a decrease in peak TIM levels in clock neurons (figure 2 in ref. 16) inconsistent with a direct role in degrading TIM. Moreover, reduction of *Cul3* on its own in vivo does not alter TIM ubiquitination (46).

We believe that our data suggest that these effects are instead due to elevated excitability/PDF signaling. Acute increases in excitability lead to acute reductions in TIM but not PER (47). Chronic activation of LNv clock neurons (via expression of the bacterial sodium channel NaChBac) results in reductions in peak levels of the CLK-activated transcription factor PDP1 (41). This effect is comparable to the reduction in peak levels in CLK-activated PER and TIM seen in *Tango10* (Fig. 3). *Cul3* has previously been shown to be required for excitation-dependent reductions in TIM (47). One possibility is that knockdown of *Cul3*, like *Tango10*, elevates excitability and thus additional excitation may not be able to further drive down TIM levels. In addition, PDF signaling is also known to feedback and regulate PER and/or TIM levels. The finding that PDF effects of *Tango10* and *Cul3* are evident even in a tim^{01} further cements the notion that core clock effects may be a secondary consequence of its excitability/PDF effects and not due to direct effects on the core clock or TIM. It is worth noting that a *clockwork orange* allele (cwo^{B9}) with comparable effects on PER and TIM oscillation amplitude in the sLNv retain more robust rhythms than observed with *Tango10* (54), suggesting the core clock effects are not sufficient for the behavioral phenotype.

We hypothesize that the primary effects of *Tango10* are on excitability, which in turn regulates PDF levels in the terminals (*SI Appendix*, Fig. S12). *Tango10* mutant lLNv exhibit an increased firing rate, possibly due to reductions in I_A current. Electrical activation of the LNv via NaChBac or TrpA1 each result in elevated PDF, as seen in *Tango10* or *Cul3* reductions (41, 42). Activity-induced increases in PDF may be further sustained by PDF release and PDFR feedback signaling (42).

Our finding of reduced I_A currents in *Tango10* mutants suggest they are a key target for mediating LNv excitability and behavior. Reduction of I_A currents elevates lLNv firing rates and alters the timing of sleep onset (48, 55). We have developed a computational model for the lLNv that more faithfully recapitulates in vivo activity, and this model demonstrates that the changes in I_A observed in *Tango10* can explain the elevated firing rates. The *Shal* transcript expression and current activity are time-dependent peaking in the evening hours, suggesting a role in mediating clock control of neuronal excitability (48, 50). These results are consistent with time-dependent effects of I_A inhibition in the evening (*SI Appendix*, Fig. S11). One possibility is that TANGO10 expression may enhance Shal currents in

NEUROSCIENCE

the evening. These effects may be conserved in mammals as reduction in I_A currents also more strongly elevate firing rates at night in the suprachiasmatic nuclei and alter circadian behavior (56, 57). I_A has also been observed to exhibit time dependence (58). It will be of interest to test the hypothesis that reductions in I_A current may result from reduced ubiquitination of Shaker/Shal ion channels or their regulators possibly via increased ion channel trafficking and/or degradation of their negative regulators.

In summary, we demonstrate a role for the BTB adapter TANGO10 in regulating LNv excitability and PDF signaling to promote circadian rhythmicity (*SI Appendix*, Fig. S12). Our behavioral, molecular, and electrophysiological data support a primary role for CUL3-TANGO10 in increasing K^+ current activity to decrease excitability. These effects on excitability can in turn regulate PDF signaling and levels to affect rhythmic behavior. Molecular clock effects may be downstream or independent of changes in excitability. Future studies will be required to determine whether CUL3/TANGO10 plays a broader role in other neuropeptidergic neurons, particularly in circadian output circuits.

Materials and Methods

***Drosophila* Strains.** All flies used this study were raised at 25 °C, 60% humidity, with standard cornmeal food under 12-h light:12-h dark (LD) cycles. Behavioral assays and immunostaining utilized male flies, except for complementation assays performed in females. Proteomic and Co-IP used a mix of males and females. w^{1118} (iso31) was used as a WT strain (Bloomington *Drosophila* Stock center, 5905). *Tango10*^{GG} (also known as *Tango10*^{GG01371}) and *Tango10* deficiency strains were also obtained from the Bloomington Stock Center [stock Nos. 12775 (*Tango10*^{GG01371}), 9171 (*Df(1)ED7147*), and 26574 (*Df(1)BSC722*)]. The *Tango10*^{GG} rhythmicity phenotype was initially identified from a screen for putative loss-of-function mutations covering 1,015 genes (44). *Tango10*^{bsr} was isolated as part of an EMS mutagenesis screen in which F1 progeny of mutagenized w^{1118} males X C(1)DX females were assayed for locomotor behavioral phenotypes (59). *Tango10*^{GG} excision strains were generated using P-element transposition. The following *Tango10* transgenic flies were generated through embryo injection by BestGene: UAS-*Tango10* (no tag), UAS-*Tango10-HA*, and UAS-*Tango10-3xFLAG*. *Tango10* RNAi (strain 103920) and UAS-*Dcr2* strains were obtained from Vienna *Drosophila* Stock Center. *Cullin-3* RNAi was obtained from National Institute of Genetics (NIG)-FLY stock center (11861R-2). *elav*-GAL4 (60), *Pdf*-GAL4 (20), *tim*-GAL4 (61), *Clk*4.1-GAL4 (62), 30Y-GAL4 (45), 247-GAL4 (63), *elav*-GAL80 (64), *Pdf*-GAL80 (65), 247-GAL80 (66), *tim*^{01} (67), *per*^{01} (68), *elav*-GeneSwitch-GAL4 (69), and *da*-GeneSwitch-GAL4 (70) were described previously.

Fly Locomotor Analysis. *Drosophila* locomotor behavioral assays were performed as described previously (71). Briefly, crosses and strains were raised at 25 °C and individual progeny were loaded into tubes containing 1% agar, 5% sucrose food, and monitored using the DAM (*Drosophila* activity monitor, Trikinetics) system under five LD cycles followed by 7 d in DD at 25 °C. Period was calculated from χ^2 periodogram using Clocklab (Actimetrics). Rhythmic power of individual fly was calculated from P-S and averaged in each genotype, and percent rhythmic was defined as percentage of flies with P-S value $\geq$ 10. For GeneSwitch crosses, 1- to 3-d-old flies were maintained on standard *Drosophila* food supplemented with 250 μM RU486 in ethanol (EtOH) or EtOH alone for 5 d. Flies were then loaded into agar-sucrose behavior tubes, again containing either RU486 or EtOH, and activity was monitored using the DAM system.

Plasmids. The coding region of *Tango10* was subcloned from DGRC, HL07962 into modified pAc5.1 (untagged, 3xHA, or 3xFLAG tags). Constructs were then subcloned into pUAS-C5 for generation of transgenic strains. The *Tango10* genomic locus, spanning 2,969 base pairs (bp) upstream and 435 bp downstream of the transcript region, was subcloned into pCasper vector. A 3xHA tag was cloned in between the C terminus of TANGO10 and the 3' untranslated region. The CUL3-V5 expression vector was described previously (44).

Antibody Generation. Rat anti-TANGO10 antibodies were generated using full length GST-TANGO10 (Cocalico Biologicals). Mouse anti-TANGO10 antibodies were generated using AKMVWGEDVP as an epitope (Abmart).

Immunohistochemistry. Flies aged ≥5 d were entrained at least 2 d before dissection. Immunostaining was performed as in ref. 7. Fly brains were dissected at the indicated time and fixed in 4% formaldehyde in phosphate-buffered saline (PBS) for 30 min at room temperature (RT). Brain samples were blocking with 5% normal goat serum in PBS containing 0.3% Triton X-100 (PBS-T) for 30 min at RT. Primary antibodies were diluted in the blocking solution and incubated in 4 °C overnight. Binding with secondary antibodies in PBS-T was done in 4 °C overnight. Samples were mounted using VECTASHIELD (Vector Labs). The antibodies used for immunostaining were as follows: mouse anti-PDF C7 (1:800, DSHB), rabbit anti-PER (1:200, gift from E.Y. Kim, Ajou University Graduate School of Medicine, Suwon, Republic of Korea), guinea pig anti-TIM [1:5,000 (72)], rat anti-HA (1:2,000, Sigma-Aldrich), rabbit anti-PDF (1:2,000, gift from J.Choe, Korea Advanced Institute of Science and Technology, Daejeon, Republic of Korea). Alexa 488, Alexa 594, and Alexa 647–conjugated secondary antibodies (Invitrogen) were diluted as 1:800. Imaging was performed by confocal microscopy using a Nikon C2 or Zeiss LSM780 confocal microscope system.

Quantification of Immunostaining. Images were processed using NIH ImageJ/Fiji. Confocal images of sLNv projections in dorsal brain regions and lLNv projections in optic lobes were z-stacked as maximum intensity projection. The intensities of anti-PDF staining above a threshold were integrated from individual z-stacked images and averaged for each genotype. Quantification of PER, TIM, and PDF in clock cells was performed as described previously (7). Arborization of PDF-positive projections was quantified by Sholl analysis using Fiji.

S2 Cell Culture. *Drosophila* Schneider 2 cells (S2-R+) (*Drosophila* Genomics Resource Center), which are derived from Oregon R late embryonic stage male tissue, were cultured in Shields and Sang M3 Insect Medium (Sigma-Aldrich) containing 10% fetal bovine serum and 1% Penicillin-Streptomycin at 25 °C. The expression plasmids were transiently transfected using Effectene (Qiagen) followed by manufacturer's protocol. Cell were harvested at 72 h post transfection.

Immunoprecipitation. Fly heads or S2 cell were lysed in T300 buffer [25 mM Tris(hydroxymethyl)aminomethane-chloride (Tris-Cl) pH 7.5, 300 mM NaCl, 10% glycerol, 1 mM ethylenediaminetetraacetic acid, 0.5% Nonidet P-40, 1 mM dithiothreitol, and 1 mM phenylmethylsulfonyl fluoride]. After centrifugation, the same volume of T0 (without NaCl from same recipe of T300) was added to lysates and bound to anti-FLAG or anti–V5 antibody–conjugated beads (Sigma-Aldrich) for 1.5 h at 4 °C. The immunoprecipitated proteins were eluted by boiling with sodium dodecyl sulfate sample buffer after three washes.

Western Blot. For immunoblotting of heads extract, 40 heads of male flies were collected and frozen at indicated time. Heads were homogenized with T300 buffer, and protein samples were loaded onto acrylamide gels. Proteins were transferred on nitrocellulose membranes (GE health), and the membranes incubated with rat anti-TANGO10 (Fig. 1 and *SI Appendix*, Fig. S4), mouse anti-TANGO10 (*SI Appendix*, Fig. S5), mouse anti-synapsin (Developmental Studies Hybridoma Bank 3C11), rat anti-GE-1 (73), mouse anti-CUL3 (BD Biosciences 611848), mouse anti-V5 (ThermoFisher), rat anti-HA (Sigma Aldrich), rabbit anti-PER (74), guinea pig anti-TIM (10), mouse anti-actin (Developmental Studies Hybridoma Bank, JLA20), and anti-FLAG (Sigma-Aldrich) antibodies. The blots were detected using enhanced chemiluminescence prime (GE Healthcare). Quantifications were performed using Image J from two separate experiments (*SI Appendix*, Fig. S5).

Proteomics. Transfected S2 cells and transgenic fly heads (*tim*-GAL4/UAS-*Tango10*-3xFLAG, *elav*-GAL4/Y; UAS-*Tango10*-3xFLAG/+) expressing triple FLAG-tagged TANGO10 were harvested and immunoprecipitated with anti-FLAG beads at ZT10 or ZT22, as in ref. 6, with $n = 1$ experiment per timepoint for each GAL4. Bound proteins were eluted using 3xFLAG peptides (Sigma). The eluted samples were subject to liquid chromatography with tandem mass spectrometry (LC-MS/MS) analysis by the Northwestern Proteomics Core Facility. The proteomics hits were identified from analysis using Proteome Discoverer software version 1.3 (Thermo Scientific), with hits for each GAL4 defined as proteins identified from either or both timepoints. Proteins identified in any GAL4-only controls were excluded. Proteins identified in proteomic analysis of FLAG-tagged TWENTY-FOUR in fly heads (6) were also removed from the hit list to improve specificity.

Electrophysiology. Brains from adult male *Drosophila* were removed from their heads in ice-cold control recording solution (in mM: 101 NaCl, 1 CaCl2, 4 MgCl2, 3 KCl, 5 glucose, 1.25 NaH_2PO_4, and 20.7 NaHCO3, pH 7.2, 250 mOsm). The connective tissue, air sacs, and trachea were removed with fine forceps. No enzymatic treatment was used to avoid removing ion channels from the cell surface. Brains were then transferred to a recording chamber and held ventral side up with a harp slice grid. Brains were allowed to rest in

continuously flowing oxygenated saline (95% oxygen and 5% carbon dioxide) for at least 10 min and no more than 2 h before recording. Perfusion with oxygenated saline was continued throughout the recording period. Time of recording is used to determine ZT.

Whole-brain electrophysiology experiments were performed on an Ultima two-photon laser scanning microscope (Bruker, formerly Prairie Technologies) equipped with galvanometers driving a Coherent Chameleon laser. Fluorescence was detected via photomultiplier tubes. Images were acquired with an upright Zeiss Axiovert microscope with a 40 × 0.9 numerical aperture water immersion objective at 512- × 512-pixels resolution and 1-μm steps. Current- and voltage-clamp recordings were performed with thick-walled borosilicate glass electrodes (1B150F-4; World Precision Instruments) ranging in resistance 10 to 14 MΩ filled with internal solution containing the following (in mM): 102 K-gluconate, 0.085 CaCl2 1.7, MgCl2, 17 NaCl, 0.94 EGTA, 8.5 Hepes, 4 Mg-ATP, 0.3 Tris-GTP, and 14 phosphocreatine (di-Tris salt), pH 7.2, 235 Osm. To visualize the recorded cell, Alexa Fluor 594 biocytin (10 μM) was added into the intracellular solution. Recordings were made using Axopatch 200B patch-clamp amplifier, digitized with a Digidata 1320 A, and acquired with pCLAMP software (Axon Instruments).

To determine firing frequency from current-clamp data, APs were detected by applying a median filter to the data, after which a set of biologically feasible thresholds were applied and used to count peaks in the signal. The most robust peaks were selected using the threshold that corresponded to the maximal voltage difference without changing the number of detected peaks. To assess membrane potential from current-clamp data, a 10th-percentile windowed filter was applied, and the membrane potential was estimated as the average of this filtered signal.

Mathematical Modeling of lLNv Electrophysiology. Our conductance-based model is based on the Smith model of LNv electrophysiology (48) and includes a voltage-gated sodium current (I_{Na}), a voltage-gated calcium current (I_{Ca}), four voltage-gated potassium currents (I_{Kv1}, I_{Kv2}, I_{Kv3}, and I_{Kv4}), a sodium leak current ($I_{leak,Na}$), and a potassium leak current ($I_{leak,K}$):

$$\begin{aligned} C\frac{dV}{dt} = I_{\text{app}} &- g_{\text{Na}} m_{\text{Na}}^3 h_{\text{Na}}(V - E_{\text{Na}}) - g_{\text{Ca}} m_{\text{Ca}} h_{\text{Ca}}(V - E_{\text{Ca}}) \\ &- g_{\text{Kv1}} m_{\text{Kv1}}^4 h_{\text{Kv1}}(V - E_{\text{K}}) - g_{\text{Kv2}} m_{\text{Kv2}}^4 (V - E_{\text{K}}) - g_{\text{Kv3}} m_{\text{Kv3}}^4 h_{\text{Kv3}}(V - E_{\text{K}}) \\ &- g_{\text{Kv4}} m_{\text{Kv4}}^4 h_{\text{Kv4}}(V - E_{\text{K}}) - g_{\text{leak, Na}}(V - E_{\text{Na}}) - g_{\text{leak, K}}(V - E_{\text{K}}) \end{aligned}$$

$$\begin{aligned} x_\infty(V) &= \frac{1}{1 + e^{-\frac{V - V_h}{k}}} \\ \tau_x(V) &= \text{Amp} \times e^{-\frac{V - V_{\max}}{\sigma}} \end{aligned}.$$

The potassium channels Shaker, Shab, Shaw, Shal are the *Drosophila* orthologs of the mammalian Kv1, Kv2, Kv3, and Kv4 channels, respectively. For the Smith model, these four potassium currents were fit to voltage-clamp data from lLNv to characterize the kinetic parameters associated with their steady state activation, x_∞, and time constants, τ_x. However in the Smith model, the kinetic parameters of the sodium and calcium currents were used unaltered from a previously published model of mammalian suprachiasmatic nucleus (SCN) neurons (49). Simulations of the Smith model show a discrepancy with our LNv recordings in terms of AP amplitude and shape (*SI Appendix*, Fig. S9), presumably due to misspecified sodium and calcium kinetics. To address this issue, we employed DA to fit the parameters of the sodium and calcium currents from current-clamp recordings of LNv. DA is a technique for obtaining optimal state and parameter estimates for dynamical models directly from observations. DA was originally developed for numerical weather prediction but has recently been utilized in neuroscience applications (75, 76). Here, we used an implementation of a variational DA algorithm previously applied to fit models to current-clamp data from SCN neurons (see ref. 77 for a detailed description of our implementation and its mathematical representation). This approach can simultaneously estimate the mean trajectory of the state variables (V, m, and h) and parameters of our model. To simplify the optimization problem, we assume a more stable form of the rate kinetics:

$$\begin{aligned} x_\infty(V) &= \frac{1}{2} + \frac{1}{2}\tanh\left(\frac{V - vx}{dvx}\right) \\ \tau_x(V) &= \tau_{x0} + \tau_{x1}\left(1 - \tanh^2\left(\frac{V - vxt}{dvxt}\right)\right) \end{aligned},$$

for $x = m_{\text{Na}}, h_{\text{Na}}, m_{\text{Ca}}, h_{\text{Ca}}$. For m_{Ca}, the time constant is assumed to be voltage independent (i.e., $\tau_x(V) = \tau_{x0}$). We are estimating each of the parameters in these equations in addition to the maximal conductances g_{Na}, g_{ca}, $g_{\text{leak, Na}}$, and $g_{\text{leak, K}}$. The Smith model has a single leak current, but here we separate the leak into sodium and potassium components as in previous SCN models (39, 78).

In variational DA, a very high-dimensional optimization problem is constructed where each model state variable, parameter, and time point adds one dimension. The fact that each time point included increases the dimension of the optimization problem, combined with the high sampling rate (10 kHz) required for current-clamp experiments to accurately capture AP waveforms, means that only a relatively small amount of data (a few seconds at most) can be assimilated before the optimization problem becomes too large to be solved. To increase the amount of information contained in these short windows of data, previous work with DA- and conductance-based models have utilized current-clamp recordings performed with complex time-varying stimuli (79) or a series of current pulses (77). In this work, we are able to fit models with DA in the absence of input currents to stimulate the neuron (i.e., using spontaneous firing activity alone). Since LNv fires slowly, there may only be one or two APs present in the short window of data that can be used for DA due to constraints on the size the optimization problem that can be solved. Thus, rather than using a raw voltage trace as the data for the DA algorithm, we elected to use an average AP waveform obtained from multiple APs in a current-clamp recording (*SI Appendix*, Fig. S10*A*). We extracted 30 APs from this trace and aligned them at the time point where the voltage crossed a spike threshold of −35 mV (*SI Appendix*, Fig. S10*B*). We then computed the mean membrane potential across these aligned APs at each point in time for a window of 350 ms prior to and 400 ms after the threshold crossing. This average AP waveform was then used as the data (observations) for our DA algorithm. The use of an average AP waveform as the observations is a contribution to DA methodology for constructing models of slow spontaneously firing neurons. We ran our DA algorithm starting from over 100 different initial conditions to select the parameters for the WT model (*SI Appendix*, Fig. S9 and Table S8). MATLAB code to perform simulations of the model is available at ModelDB (https://senselab.med.yale.edu/modeldb/).

Data Availability. The mass spectrometry proteomics data have been deposited to the ProteomeXchange Consortium via the PRIDE partner repository with the dataset identifier PXD029326.

ACKNOWLEDGMENTS. We thank Joonho Choe, Eun Young Kim, Bloomington *Drosophila* Stock Center, Vienna *Drosophila* Stock Center, NIG-FLY Stock Center, *Drosophila* Genomics Resource Center, and Developmental Studies Hybridoma Bank for reagents; Northwestern Proteomics Core Facility for LC-MS/MS analysis. This work was supported by grants from the NIH (Grants R01NS106955, R56NS052903, and HL7909-19) and Defense Advanced Research Projects Agency (Grant D12AP0023 [R.A.]), the National Research Foundation, Republic of Korea (Grant NRF-2019R1I1A1A01063087 [J.L.]; Grant NRF-2021M3A9G8022960 [C.L.]), the NSF (Grant DMS 1555237) [C.O.D.], the Department of the Army—Materiel Command (Grant W911NF1610584 [R.A., W.L.K., and C.O.D.]), and the Simons Foundation Autism Research Initiative (Grant 735135).

1. R. Allada, N. E. White, W. V. So, J. C. Hall, M. Rosbash, A mutant Drosophila homolog of mammalian Clock disrupts circadian rhythms and transcription of period and timeless. *Cell* **93**, 791–804 (1998).
2. J. E. Rutila *et al.*, CYCLE is a second bHLH-PAS clock protein essential for circadian rhythmicity and transcription of Drosophila period and timeless. *Cell* **93**, 805–814 (1998).
3. S. A. Cyran *et al.*, vrille, Pdp1, and dClock form a second feedback loop in the Drosophila circadian clock. *Cell* **112**, 329–341 (2003).
4. N. R. Glossop *et al.*, VRILLE feeds back to control circadian transcription of Clock in the Drosophila circadian oscillator. *Neuron* **37**, 249–261 (2003).
5. S. Kojima, D. L. Shingle, C. B. Green, Post-transcriptional control of circadian rhythms. *J. Cell Sci.* **124**, 311–320 (2011).
6. C. Lim, R. Allada, ATAXIN-2 activates PERIOD translation to sustain circadian rhythms in Drosophila. *Science* **340**, 875–879 (2013).
7. C. Lim *et al.*, The novel gene twenty-four defines a critical translational step in the Drosophila clock. *Nature* **470**, 399–403 (2011).
8. C. Lim, R. Allada, Emerging roles for post-transcriptional regulation in circadian clocks. *Nat. Neurosci.* **16**, 1544–1550 (2013).
9. Y. Zhang, J. Ling, C. Yuan, R. Dubruille, P. Emery, A role for Drosophila ATX2 in activation of PER translation and circadian behavior. *Science* **340**, 879–882 (2013).
10. C. Lim *et al.*, Functional role of CREB-binding protein in the circadian clock system of Drosophila melanogaster. *Mol. Cell. Biol.* **27**, 4876–4890 (2007).
11. H. W. Ko, J. Jiang, I. Edery, Role for Slimb in the degradation of Drosophila period protein phosphorylated by Doubletime. *Nature* **420**, 673–678 (2002).
12. B. Grima *et al.*, The F-box protein slimb controls the levels of clock proteins period and timeless. *Nature* **420**, 178–182 (2002).
13. K. Koh, X. Zheng, A. Sehgal, JETLAG resets the Drosophila circadian clock by promoting light-induced degradation of TIMELESS. *Science* **312**, 1809–1812 (2006).

14. N. Peschel, S. Veleri, R. Stanewsky, Veela defines a molecular link between Cryptochrome and timeless in the light-input pathway to Drosophila's circadian clock. *Proc. Natl. Acad. Sci. U.S.A.* **103**, 17313–17318 (2006).
15. N. Peschel, K. F. Chen, G. Szabo, R. Stanewsky, Light-dependent interactions between the Drosophila circadian clock factors cryptochrome, jetlag, and timeless. *Curr. Biol.* **19**, 241–247 (2009).
16. B. Grima, A. Dognon, A. Lamouroux, E. Chélot, F. Rouyer, CULLIN-3 controls TIMELESS oscillations in the Drosophila circadian clock. *PLoS Biol.* **10**, e1001367 (2012).
17. Y. Peng, D. Stoleru, J. D. Levine, J. C. Hall, M. Rosbash, Drosophila free-running rhythms require intercellular communication. *PLoS Biol.* **1**, E13 (2003).
18. Y. Lin, G. D. Stormo, P. H. Taghert, The neuropeptide pigment-dispersing factor coordinates pacemaker interactions in the Drosophila circadian system. *J. Neurosci.* **24**, 7951–7957 (2004).
19. D. Stoleru, Y. Peng, P. Nawathean, M. Rosbash, A resetting signal between Drosophila pacemakers synchronizes morning and evening activity. *Nature* **438**, 238–242 (2005).
20. S. C. Renn, J. H. Park, M. Rosbash, J. C. Hall, P. H. Taghert, A pdf neuropeptide gene mutation and ablation of PDF neurons each cause severe abnormalities of behavioral circadian rhythms in Drosophila. *Cell* **99**, 791–802 (1999).
21. B. C. Lear *et al.*, A G protein-coupled receptor, groom-of-PDF, is required for PDF neuron action in circadian behavior. *Neuron* **48**, 221–227 (2005).
22. S. Hyun *et al.*, Drosophila GPCR Han is a receptor for the circadian clock neuropeptide PDF. *Neuron* **48**, 267–278 (2005).
23. I. Mertens *et al.*, PDF receptor signaling in Drosophila contributes to both circadian and geotactic behaviors. *Neuron* **48**, 213–219 (2005).
24. S. H. Im, W. Li, P. H. Taghert, PDFR and CRY signaling converge in a subset of clock neurons to modulate the amplitude and phase of circadian behavior in Drosophila. *PLoS One* **6**, e18974 (2011).
25. J. H. Park *et al.*, Differential regulation of circadian pacemaker output by separate clock genes in Drosophila. *Proc. Natl. Acad. Sci. U.S.A.* **97**, 3608–3613 (2000).
26. J. Blau, M. W. Young, Cycling vrille expression is required for a functional Drosophila clock. *Cell* **99**, 661–671 (1999).
27. K. L. Gunawardhana, P. E. Hardin, VRILLE controls PDF neuropeptide accumulation and arborization rhythms in small ventrolateral neurons to drive rhythmic behavior in Drosophila. *Curr. Biol.* **27**, 3442–3453.e4 (2017).
28. B. C. Lear *et al.*, The ion channel narrow abdomen is critical for neural output of the Drosophila circadian pacemaker. *Neuron* **48**, 965–976 (2005).
29. W. Luo *et al.*, NonA and CPX Link the circadian clockwork to locomotor activity in Drosophila. *Neuron* **99**, 768–780.e3 (2018).
30. M. P. Fernández *et al.*, Impaired clock output by altered connectivity in the circadian network. *Proc. Natl. Acad. Sci. U.S.A.* **104**, 5650–5655 (2007).
31. F. J. Blanchard *et al.*, The transcription factor Mef2 is required for normal circadian behavior in Drosophila. *J. Neurosci.* **30**, 5855–5865 (2010).
32. K. C. Abruzzi *et al.*, Drosophila clock target gene characterization: Implications for circadian tissue-specific gene expression. *Genes Dev.* **25**, 2374–2386 (2011).
33. A. Sivachenko, Y. Li, K. C. Abruzzi, M. Rosbash, The transcription factor Mef2 links the Drosophila core clock to Fas2, neuronal morphology, and circadian behavior. *Neuron* **79**, 281–292 (2013).
34. A. Petsakou, T. P. Sapsis, J. Blau, Circadian rhythms in Rho1 activity regulate neuronal plasticity and network hierarchy. *Cell* **162**, 823–835 (2015).
35. M. P. Fernandez *et al.*, Sites of circadian clock neuron plasticity mediate sensory integration and entrainment. *Curr. Biol.* **30**, 2225–2237.e5 (2020).
36. E. Kula, E. S. Levitan, E. Pyza, M. Rosbash, PDF cycling in the dorsal protocerebrum of the Drosophila brain is not necessary for circadian clock function. *J. Biol. Rhythms* **21**, 104–117 (2006).
37. V. Sheeba, H. Gu, V. K. Sharma, D. K. O'Dowd, T. C. Holmes, Circadian- and light-dependent regulation of resting membrane potential and spontaneous action potential firing of Drosophila circadian pacemaker neurons. *J. Neurophysiol.* **99**, 976–988 (2008).
38. G. Cao, M. N. Nitabach, Circadian control of membrane excitability in Drosophila melanogaster lateral ventral clock neurons. *J. Neurosci.* **28**, 6493–6501 (2008).
39. M. Flourakis *et al.*, A conserved bicycle model for circadian clock control of membrane excitability. *Cell* **162**, 836–848 (2015).
40. M. F. Ceriani *et al.*, Genome-wide expression analysis in Drosophila reveals genes controlling circadian behavior. *J. Neurosci.* **22**, 9305–9319 (2002).
41. M. N. Nitabach *et al.*, Electrical hyperexcitation of lateral ventral pacemaker neurons desynchronizes downstream circadian oscillators in the fly circadian circuit and induces multiple behavioral periods. *J. Neurosci.* **26**, 479–489 (2006).
42. A. Herrero *et al.*, Coupling neuropeptide levels to structural plasticity in Drosophila clock neurons. *Curr. Biol.* **30**, 3154–3166.e4 (2020).
43. A. Depetris-Chauvin *et al.*, Adult-specific electrical silencing of pacemaker neurons uncouples molecular clock from circadian outputs. *Curr. Biol.* **21**, 1783–1793 (2011).
44. C. Pfeiffenberger, R. Allada, Cul3 and the BTB adaptor insomniac are key regulators of sleep homeostasis and a dopamine arousal pathway in Drosophila. *PLoS Genet.* **8**, e1003003 (2012).
45. M. Y. Yang, J. D. Armstrong, I. Vilinsky, N. J. Strausfeld, K. Kaiser, Subdivision of the Drosophila mushroom bodies by enhancer-trap expression patterns. *Neuron* **15**, 45–54 (1995).
46. Á. Szabó *et al.*, Ubiquitylation dynamics of the clock cell proteome and TIMELESS during a circadian cycle. *Cell Rep.* **23**, 2273–2282 (2018).
47. F. Guo, I. Cerullo, X. Chen, M. Rosbash, PDF neuron firing phase-shifts key circadian activity neurons in Drosophila. *eLife* **3**, e02780 (2014).
48. P. Smith, E. Buhl, K. Tsaneva-Atanasova, J. J. L. Hodge, Shaw and Shal voltage-gated potassium channels mediate circadian changes in Drosophila clock neuron excitability. *J. Physiol.* **597**, 5707–5722 (2019).
49. C. K. Sim, D. B. Forger, Modeling the electrophysiology of suprachiasmatic nucleus neurons. *J. Biol. Rhythms* **22**, 445–453 (2007).
50. E. Kula-Eversole *et al.*, Surprising gene expression patterns within and between PDF-containing circadian neurons in Drosophila. *Proc. Natl. Acad. Sci. U.S.A.* **107**, 13497–13502 (2010).
51. B. C. Lear *et al.*, UNC79 and UNC80, putative auxiliary subunits of the NARROW ABDOMEN ion channel, are indispensable for robust circadian locomotor rhythms in Drosophila. *PLoS One* **8**, e78147 (2013).
52. N. Foot, T. Henshall, S. Kumar, Ubiquitination and the regulation of membrane proteins. *Physiol. Rev.* **97**, 253–281 (2017).
53. M. Gschweitl *et al.*, A SPOPL/Cullin-3 ubiquitin ligase complex regulates endocytic trafficking by targeting EPS15 at endosomes. *eLife* **5**, e13841 (2016).
54. B. Richier, C. Michard-Vanhée, A. Lamouroux, C. Papin, F. Rouyer, The clockwork orange Drosophila protein functions as both an activator and a repressor of clock gene expression. *J. Biol. Rhythms* **23**, 103–116 (2008).
55. G. Feng *et al.*, Control of sleep onset by Shal/K_v4 channels in *Drosophila* circadian neurons. *J. Neurosci.* **38**, 9059–9071 (2018).
56. D. Granados-Fuentes, A. J. Norris, Y. Carrasquillo, J. M. Nerbonne, E. D. Herzog, I(A) channels encoded by Kv1.4 and Kv4.2 regulate neuronal firing in the suprachiasmatic nucleus and circadian rhythms in locomotor activity. *J. Neurosci.* **32**, 10045–10052 (2012).
57. T. O. Hermanstyne, D. Granados-Fuentes, R. L. Mellor, E. D. Herzog, J. M. Nerbonne, Acute knockdown of Kv4.1 regulates repetitive firing rates and clock gene expression in the suprachiasmatic nucleus and daily rhythms in locomotor behavior. *eNeuro* **4**, ENEURO.0377-16.2017 (2017).
58. J. N. Itri *et al.*, Circadian regulation of a-type potassium currents in the suprachiasmatic nucleus. *J. Neurophysiol.* **103**, 632–640 (2010).
59. C. Bökel, EMS screens: From mutagenesis to screening and mapping. *Methods Mol. Biol.* **420**, 119–138 (2008).
60. D. M. Lin, C. S. Goodman, Ectopic and increased expression of Fasciclin II alters motoneuron growth cone guidance. *Neuron* **13**, 507–523 (1994).
61. M. Kaneko, J. C. Hall, Neuroanatomy of cells expressing clock genes in Drosophila: Transgenic manipulation of the period and timeless genes to mark the perikarya of circadian pacemaker neurons and their projections. *J. Comp. Neurol.* **422**, 66–94 (2000).
62. L. Zhang *et al.*, DN1(p) circadian neurons coordinate acute light and PDF inputs to produce robust daily behavior in Drosophila. *Curr. Biol.* **20**, 591–599 (2010).
63. T. Zars, M. Fischer, R. Schulz, M. Heisenberg, Localization of a short-term memory in Drosophila. *Science* **288**, 672–675 (2000).
64. E. J. Rideout, A. J. Dornan, M. C. Neville, S. Eadie, S. F. Goodwin, Control of sexual differentiation and behavior by the doublesex gene in Drosophila melanogaster. *Nat. Neurosci.* **13**, 458–466 (2010).
65. D. Stoleru, Y. Peng, J. Agosto, M. Rosbash, Coupled oscillators control morning and evening locomotor behaviour of Drosophila. *Nature* **431**, 862–868 (2004).
66. M. J. Krashes, A. C. Keene, B. Leung, J. D. Armstrong, S. Waddell, Sequential use of mushroom body neuron subsets during Drosophila odor memory processing. *Neuron* **53**, 103–115 (2007).
67. A. Sehgal, J. L. Price, B. Man, M. W. Young, Loss of circadian behavioral rhythms and per RNA oscillations in the Drosophila mutant timeless. *Science* **263**, 1603–1606 (1994).
68. R. J. Konopka, S. Benzer, Clock mutants of Drosophila melanogaster. *Proc. Natl. Acad. Sci. U.S.A.* **68**, 2112–2116 (1971).
69. T. Osterwalder, K. S. Yoon, B. H. White, H. Keshishian, A conditional tissue-specific transgene expression system using inducible GAL4. *Proc. Natl. Acad. Sci. U.S.A.* **98**, 12596–12601 (2001).
70. H. Tricoire *et al.*, The steroid hormone receptor EcR finely modulates Drosophila lifespan during adulthood in a sex-specific manner. *Mech. Ageing Dev.* **130**, 547–552 (2009).
71. C. Lim *et al.*, Clockwork orange encodes a transcriptional repressor important for circadian-clock amplitude in Drosophila. *Curr. Biol.* **17**, 1082–1089 (2007).
72. B. Barbagallo, H. A. Prescott, P. Boyle, J. Climer, M. M. Francis, A dominant mutation in a neuronal acetylcholine receptor subunit leads to motor neuron degeneration in Caenorhabditis elegans. *J. Neurosci.* **30**, 13932–13942 (2010).
73. A. Eulalio, I. Behm-Ansmant, D. Schweizer, E. Izaurralde, P-body formation is a consequence, not the cause, of RNA-mediated gene silencing. *Mol. Cell. Biol.* **27**, 3970–3981 (2007).
74. R. Stanewsky *et al.*, Temporal and spatial expression patterns of transgenes containing increasing amounts of the Drosophila clock gene period and a lacZ reporter: Mapping elements of the PER protein involved in circadian cycling. *J. Neurosci.* **17**, 676–696 (1997).
75. S. J. Schiff, *Neural Control Engineering: The Emerging Intersection Between Control Theory and Neuroscience* (MIT Press, Cambridge, MA, 2012).
76. M. J. Moye, C. O. Diekman, Data assimilation methods for neuronal state and parameter estimation. *J. Math. Neurosci.* **8**, 11 (2018).
77. B. Bano-Otalora, J. A. Madrid, M. A. Rol, Melatonin alleviates circadian system disruption induced by chronic shifts of the light-dark cycle in Octodon degus. *J. Pineal Res.* **68**, e12619 (2020).
78. C. O. Diekman *et al.*, Causes and consequences of hyperexcitation in central clock neurons. *PLOS Comput. Biol.* **9**, e1003196 (2013).
79. C. D. Meliza *et al.*, Estimating parameters and predicting membrane voltages with conductance-based neuron models. *Biol. Cybern.* **108**, 495–516 (2014).